Sperm chemotaxis is driven by the slope of the chemoattractant concentration field

Ramírez-Gómez H.V.[1], Jimenez Sabinina V.[2], Velázquez-Pérez M.[1], Beltrán C.[1], Carneiro J.[3], Wood C.D.[1, 4], Tuval I.[5], Darszon A.[1, *], Guerrero A.[1, 4, *].

[1] Departamento de Genética del Desarrollo y Fisiología Molecular, Instituto de Biotecnología, Universidad Nacional Autónoma de México (UNAM), Cuernavaca, Morelos, 62210, México.

[2] Cell Biology and Biophysics Unit, European Molecular Biology Laboratory (EMBL), Heidelberg, Germany.

[3] Instituto Gulbenkian de Ciência (IGC), Rua da Quinta Grande, 6 2780-156, Oeiras, Portugal.

[4] Laboratorio Nacional de Microscopía Avanzada, Instituto de Biotecnología, Universidad Nacional Autónoma de México (UNAM), Cuernavaca, Morelos, 62210, México.

[5] Mediterranean Institute for Advanced Studies, IMEDEA (CSIC-UIB), Esporles, Balearic Islands, Spain.

[*] Correspondence and requests should be addressed to A.G. or A.D. (email: adanog@ibt.unam.mx, darszon@ibt.unam.mx).

Abstract

Spermatozoa are attracted to their conspecific female gamete by diffusive molecules released from the egg investments in a process called chemotaxis. The decapeptide speract induces metabolic and permeability changes in *Strongylocentrotus purpuratus* sea urchin sperm. In the decades since speract purification from *S. purpuratus* egg investments, sperm chemotaxis has not been demonstrated in this species. By studying how the stimulus function, which spermatozoa experience during the accumulation of bound chemoattractants throughout their trajectory, influences both their motility response and their internal Ca^{2+} oscillations, we were able to show that *S. purpuratus* spermatozoa exhibit chemotaxis under sufficiently steep speract concentration gradients. We demonstrate that this process arises through frequency entrainment of the coupled metabolic oscillators.

Introduction

Broadcast spawning organisms, such as marine invertebrates, release their gametes into open sea, where they are often subject to extensive dilution that reduces the probability of gamete encounter (Lotterhos et al., 2010). In many marine organisms, female gametes release diffusible molecules that attract homologous spermatozoa (Lillie, 1913; Miller, 1985; Suzuki, 1995). Propelled by their beating flagella, spermatozoa detect and respond to chemoattractant concentration gradients by steering their swimming trajectory toward the gradient source: the egg. Though it was in bracken ferns where sperm chemotaxis was first identified (Pfeffer, 1884), sea urchins are currently the best-characterized model system for studying sperm chemotaxis at a molecular level (Alvarez et al., 2012; Cook et al., 1994; Darszon et al., 2008; Strünker et al., 2015; Wood et al., 2015).

The sea urchin egg is surrounded by an extracellular matrix which contains short sperm-activating peptides (SAPs), that modulate sperm motility through altering intracellular Ca^{2+} concentration ($[Ca^{2+}]_i$) and other signaling intermediates (Darszon et al., 2008; Suzuki, 1995). The probability of sperm-egg encounter is enhanced by the prompt transduction of the biochemical signals triggered by SAPs into the appropriate reorientation of the sperm trajectory.

The decapeptide speract is one of best characterized members of the SAP family due to its powerful stimulating effect on metabolism, permeability and motility in *Strongylocentrotus purpuratus* and *Lytechinus pictus* spermatozoa. The binding of speract to its receptor located in the flagellar plasma membrane, triggers a train of $[Ca^{2+}]_i$ increases in immobilized *S. purpuratus* spermatozoa (Wood et al., 2003). This calcium signal was proposed to regulate the activity of dynein motor proteins in the flagellum, and thus potentially modulate the trajectory of free-swimming spermatozoa (Brokaw, 1979).

A direct link between $[Ca^{2+}]_i$ signaling and sperm motility was established through the use of optochemical techniques to rapidly, and non-turbulently, expose swimming sea urchin spermatozoa to their conspecific attractant in a well-controlled experimental regime (Böhmer et al., 2005; Wood et al., 2005). Currently, it is well established that the transient $[Ca^{2+}]_i$ increases triggered by chemoattractants produce a sequence of turns and straight swimming episodes (turn-and-run), where each turning event results from the rapid increase in the $[Ca^{2+}]_i$ (Alvarez et al., 2012; Böhmer et al., 2005; Shiba et al., 2008; Wood et al., 2005). The turn-and-run response seems to be a general requirement for sperm chemotaxis in sea urchins, however it is not sufficient on its own to produce a chemotactic response (Guerrero et al., 2010; Strünker et al., 2015; Wood et al., 2007, 2005).

Our current understanding of chemotaxis, suggests that sperm first sample the chemoattractant concentration gradient while swimming in periodic paths (either circular 2D or helical 3D). During the sampling phase, the accumulation of bound chemoattractants triggers $[Ca^{2+}]_i$ transients that control the symmetry of the waveform of the flagellar beat. In this way, the alternate periods of asymmetrical (turn) and symmetrical (run) flagellar beating give rise to a looping swimming pattern that guides cells to the source of the chemoattractant gradient.

Friedrich and Jülicher proposed a generic theory that captures the essence of sperm navigation following periodic paths in a non-homogeneous chemoattractant field, in which the sampling of a periodic concentration stimulus $s(t)$ is translated by intracellular signaling $i(t)$ into the periodic modulation of the swimming path curvature $k(t)$ (Friedrich and Jülicher, 2008, 2007). As result, the periodic swimming path drifts in a direction that depends on the internal dynamics of the signaling system. In this theory, the latency of the

intracellular signaling (i.e. the $[Ca^{2+}]_i$ signal), expressed as the phase shift between *s(t)* and *k(t)*, is a crucial determinant of the directed looping of the swimming trajectory up the chemical concentration field. This theory also predicts that chemotaxis is a robust property of the system that does not require fine-tuning of parameters if the signaling system is adaptive (Friedrich and Jülicher, 2009, 2008). In other words, there is a large range of parameters for which sperm chemotaxis is a robust outcome, providing an effective way for sampling the local chemoattractant concentration field and detecting the direction of the concentration gradient (Friedrich and Jülicher, 2008, 2007; Kashikar et al., 2012; Kaupp et al., 2003; Pichlo et al., 2014).

Even though the conceptual framework of Friedrich & Jülicher provides insights into the mechanism governing sperm chemotaxis, it does not explore the scenario whereby chemoattractants trigger an autonomous $[Ca^{2+}]_i$ oscillator operating in the absence of a periodic stimulus. The existence of an autonomous $[Ca^{2+}]_i$ oscillator triggered by chemoattractants (Aguilera et al., 2012; Espinal et al., 2011; Wood et al., 2003) suggests that sperm chemotaxis might operate in a dynamical space where two autonomous oscillators, namely the stimulus function and the internal Ca^{2+} oscillator, reach frequency entrainment.

In spite of 30 years of research since speract's isolation from *S. purpuratus* oocytes (Hansbrough and Garbers, 1981; Suzuki, 1995), chemotaxis of *S. purpuratus* sperm towards this peptide has not yet been demonstrated (Cook et al., 1994; Darszon et al., 2008; Guerrero et al., 2010; Kaupp, 2012; Miller, 1985; Wood et al., 2015). A comparison between individual *L. pictus* and *S. purpuratus* sperm responses to a specific chemoattractant concentration gradient generated by photoactivating caged speract (CS) revealed that only *L. pictus* spermatozoa exhibit chemotaxis under these conditions

(Guerrero et al., 2010). In that study, *L. pictus* spermatozoa experience $[Ca^{2+}]_i$ fluctuations and pronounced turns while swimming in descending speract gradients, that result in spermatozoa reorienting their swimming behavior along the positive chemoattractant concentration gradient. In contrast, *S. purpuratus* spermatozoa experience similar trains of $[Ca^{2+}]_i$ fluctuations that in turn drive them to relocate, but with no preference towards the center of the chemoattractant gradient (Guerrero et al., 2010).

In the present work, we investigate whether *S. purpuratus* spermatozoa can undergo chemotaxis. Particularly, we examined whether the chemoattractant concentration gradient has to have a minimum steepness to be adequately detected. If true, this limit may have prevented the observation and characterization of their chemotactic response to date. We report that *S. purpuratus* spermatozoa are chemotactic only when exposed to much steeper speract concentration gradients than those previously employed. Furthermore, we have explored the coupling between the recruitment of speract molecules during sperm translation, and the internal Ca^{2+} oscillator; and demonstrate that sperm chemotaxis arises through coupled metabolic oscillators.

Results

Constraints upon the detection of chemoattractant concentration fields

To examine why so far *S. purpuratus* spermatozoa have not been shown to be chemotactic, we asked ourselves what limits this response? The challenge for a sperm that must swim towards higher stimulus intensities (i.e. up a chemoattractant concentration gradient) is to determine the direction in which the intensity increases or decreases during its journey (Dusenbery, 2011). To do so, the minimum requirement is to detect the intensity of the stimulus at two distinct locations, and act on the expectation that the gradient continues beyond the limits of the measurement (**Figure 1a**).

To reliably measure a concentration gradient of chemoattractant, this difference in binding events detected by the spermatozoon in the measurement interval must be above the noise level (**Figure 1a**). Considering the biophysical constraints of the case in question, the probability that a spermatozoon has to detect a gradient of diffusible molecules depends of the sperm velocity (v), the sampling time (t_{int}), the number of receptors (N), the radius of the receptor binding pocket (s), the size of the cell (a), the diffusion constant of the chemoattractant (D), the concentration of the chemoattractant (c), and the slope of the chemoattractant gradient (ξ) (**Figure 1a**, **Table S1**, for further explanation see **Theory 2.4. Uncertainty in the detection of a chemoattractant concentration fields**, in **supplementary materials**). The associated uncertainty to reliable determine the direction of the chemoattractant gradient u_2, can be expressed as:

$$u_2 = v^{-1} {t_{int}}^{-3/2} \left(\frac{Ns}{Ns+\pi a} D\right)^{-1/2} c^{1/2} \xi^{-1} \ll 1 \qquad (1)$$

Equation (**1**) indicates that the slope of the chemoattractant concentration gradient, $\xi = dc/dr$, directly impinges on the ability to reliably determine the source of the

attractant, being indirectly proportional to the uncertainty. In other words, the uncertainty associated with the detection of a large (i.e. steep) gradient is very low, and vice versa. The quantity ξ has units of concentration over distance, and it is indicative of the strength of the stimuli received when sampling a particular location r_1 and r_2, each with a given chemoattractant concentration c_1 and c_2 (**Figure 1a**). Typically, $dc = c_2 - c_1$ is in the order of picomolar and $dr = r_2 - r_1$ in microns. As ξ increases, the strength of chemotactic signal increases. In contrast, homogeneous concentration gradients are characterized by $c_1 \sim c_2$, hence there is no positional information for sperm guidance, where $dc \rightarrow 0$.

The least fractional error attainable in the determination of chemoattractant gradient direction u_2, has no upper boundary, however values greater than 1 indicate that stochastic fluctuations dominate over the signal. For simplicity, u_2 will be considered to operate in the range [0, 1].

We modeled the uncertainties for different gradients (10^{-11} to 10^{-6} M) for the three sea urchin species. At high concentrations of speract (10^{-8} to 10^{-6} M) the change in receptor occupancy experienced by *L. pictus* spermatozoa, at two given distinct locations, allows the reliable assessment of relatively shallow chemical gradients, with u_2 below 0.01 for a wide range of ξ (**Figure 1c**). However, at low concentrations of speract (below 10^{-10} M), keeping all other parameters equal, stochastic fluctuations tend to dominate over the signal. In this low-concentration regime, the slope of the chemoattractant gradient is determinant. Shallow gradients ($\xi < 10^{-12}$ M μm^{-1}) increase the uncertainty for detection of gradient polarity, while steeper chemoattractant gradients allow *L. pictus* spermatozoa to determine the orientation of the chemical gradient dependably (**Figure 1c**, orange and brown lines with u_2

< 1%). In contrast to *L. pictus*, taking into account the previous considerations, *S. purpuratus* spermatozoa can only determine the orientation of the chemical gradient for high enough speract concentrations and steep, but not shallow, concentration gradients (**Figure 1b**, only orange line with $u_2 < 1\%$).

Noteworthy, our calculations indicate that in *S. purpuratus* and *L. pictus* spermatozoa act in a regime where the rate of chemoattractant uptake is slower than diffusion, then they cannot be considered as perfect absorbers, the actual number of speract receptors for both species is significantly lower than $N_{1/2} \sim 3\text{x}10^5$, which is the required receptor number for being a perfect absorber. Moreover, we show that such observation holds when considering the cylindrical geometry of the sperm flagellum (**Figure S1, Table S1,** and **Theory *2.2. On the estimate of maximal chemoattractant absorption***, in **supplementary materials**) (Nishigaki et al., 2001; Nishigaki and Darszon, 2000). The later suggests that the differences in the number of receptors amongst these species may contribute to their differential sensitivity to reliably determine the direction of the chemoattractant gradient.

To understand the differential sensitivity between the spermatozoa of *S. purpuratus* and *L. pictus*, we analyzed the scenario in which the probabilities of the detection of the gradient for both spermatozoa species were equal, i.e. they would have the same uncertainties $u_{purpuratus} = u_{pictus}$. After mathematical simplification, we compute the ratio between the slopes of the gradient of both species, which represents a scaling factor (*SF*) in the gradient slope between *S. purpuratus* and *L. pictu*s spermatozoa, expressed as:

$$SF = \frac{\xi_{purpuratus}}{\xi_{pictus}} = \left(\frac{v_{purpuratus}}{v_{pictus}}\right)^{-1} \left(\frac{t_{purpuratus}}{t_{pictus}}\right)^{-3/2} \left(\frac{Z_{purpuratus}}{Z_{pictus}}\right)^{-1/2} \sim 3 \qquad (2)$$

Where $Z = \left(\frac{Ns}{Ns + \pi a}\right)$ is the probability that a molecule that has collided with the cell will find a receptor (Berg and Purcell, 1977), which represents the area fraction of the cell

covered by chemoattractant receptors, and *SF* is a factor that scales the slope of the speract gradient to a regime that allows *S. purpuratus* spermatozoa to detect the local direction of the chemical gradient with the same uncertainty as the *L. pictus* spermatozoa would. In other words, the model predicts that *S. purpuratus* spermatozoa should undergo chemotaxis in a speract gradient approximately three times steeper than the gradient that drives chemotaxis in *L. pictus* spermatozoa, with $\xi_{purpuratus} \sim 3\xi_{pictus}$.

In summary, the chemoreception model suggests that *S. purpuratus* spermatozoa detect chemoattractant gradients with less sensitivity than those of *L. pictus*. It also predicts that *S. purpuratus* spermatozoa may detect chemoattractant gradients in the 10^{-9} M regime with sufficient certainty only if the difference in sampling concentration is greater than 10^{-11} M μm^{-1} (i.e. steep concentration gradients). If the latter holds to be true, then *S. purpuratus* spermatozoa should be able to experience chemotaxis when exposed to steeper speract gradients than those tested experimentally so far. Given this prediction, we designed and implemented an experimental condition for which we expect *S. purpuratus* spermatozoa to experience chemotaxis.

S. purpuratus spermatozoa accumulate at steep speract concentration gradients

Our experimental setup is designed to generate specific concentration gradients by focusing a brief (200 ms) flash of UV light along an optical fiber, through the objective, and into a field of swimming *S. purpuratus* spermatozoa containing caged-speract (CS) at 10 nM in artificial sea water (Guerrero et al., 2010; Tatsu et al., 2002). To test experimentally whether *S. purpuratus* spermatozoa undergo chemotaxis, as predicted from the chemoreception model, we varied the slope of the chemoattractant gradient by

separately employing four optical fibers of distinct diameters that could be arranged into five different configurations (*f1, f2, f3, f4, f5*) (**Figure 2c**).

Each configuration produces a characteristic pattern of UV illumination within the imaging field (**Figure 2**). The UV intensity was measured at the back focal plane of the objective for each fiber configuration (**Table S2**). The spatial derivative of the imaged UV light profile was computed for use as a proxy for the slope of the speract concentration gradient (**Figure 2b**). By examining these UV irradiation patterns, the highest concentration of speract released through photo-liberation from CS is generated by the *f5* fiber, followed by *f4* > *f3* > *f2* > *f1* (**Figure 2a**). The steepest UV irradiation gradients are those generated by the *f2, f3* and *f5* fibers (**Figure 2b**).

Irrespective of the optical fiber used, the photo-activation of caged speract triggers the stereotypical Ca^{2+}-dependent motility responses of *S. purpuratus* spermatozoa **(Figure 2d, Movies 1, S1, S4, S5** and **S6**). To determine whether these changes lead to sperm accumulation, we developed an algorithm which automatically scores the number of spermatozoa at any of four defined concentric regions (R1, R2, R3, and R4) relative to the center of the speract concentration gradient (**Figure S3**).

Photo-liberation of speract through either the *f2* or *f3* fibers, but not through the *f1, f4* or *f5* fibers, lead to the accumulation of *S. purpuratus* spermatozoa towards the center of the speract gradient (zones R1 and R2) within the first 5-10 seconds after UV irradiation (**Figure 3a**, **S4**, **Movies 1**, and **S1**).

Interestingly, for *f2*, the number of spermatozoa increases in R1 and R2 and decreases in R3 and R4, indicating that cells from the R3 and R4 regions most probably relocate towards R1 and R2 (**Figure 3a**, **S4,** and **Movie 1**). In the case of the *f3* gradient, the number of spermatozoa increases in the R1, R2 and R3 regions and decreases in the R4 region,

suggesting that spermatozoa in R4 and possibly outside of the imaged field are entering the other regions (**Figure 3a** and **Movie S2**). The maximum sperm accumulation (about two-fold) occurs in R1 for the *f3* gradient (**Figure 3a**).

In the case of exposure to the speract concentration gradient generated by illumination through the *f5* fiber, the number of spermatozoa showed a tendency to increase in R2, R3 and R4 (**Figure 3a**, **S4,** and **Movie S6)**. Gradients *f1, f4* and negative controls (Low $[Ca^{2+}]_i$ or High extracellular K^+ ($[K^+]_e$)) did not show increased sperm numbers in any region (**Figure 3a**, **S4**, **Movies S4, S5, S2** and **S3**, respectively).

We also evaluated the corresponding $[Ca^{2+}]_i$ changes across the imaging field for each imposed speract concentration gradient. Gradients *f2* to *f5* increase $[Ca^{2+}]_i$ in spermatozoa at least two-fold, while the increase for the *f1* gradient was modest (**Figure 3b**). Interestingly, $[Ca^{2+}]_i$ levels rose highest upon exposure to the *f4* gradient, even though the number of spermatozoa did not increase significantly (**Figure 3a**), which underlines the notion that elevated $[Ca^{2+}]_i$ levels are necessary, but not sufficient to drive the accumulation of spermatozoa (**Figure 3**), as previously suggested (Alvarez et al., 2012; Böhmer et al., 2005; Guerrero et al., 2010; Kaupp et al., 2003; Wood et al., 2005).

In summary, *S. purpuratus* spermatozoa significantly accumulate towards the center of the speract gradients generated by the *f2*- and *f3*-fibers, which are the two that generate UV light profiles with steeper slopes compared to the *f1* and *f4* fibers (**Figure 2b**). Notably, use of fibers *f4* and *f5* uncages higher concentrations of speract (by providing higher UV energies than other fibers) (**Figure 2a, Table S2**), yet they do not trigger the maximum accumulation of *S. purpuratus* spermatozoa at the center of the chemoattractant field.

S. purpuratus spermatozoa undergo chemotaxis upon exposure to steep speract gradients

The spatial derivative of the UV profiles shown in **Figure 2b** indicates that the steeper light gradients generated from UV irradiation are those of *f2, f3* and *f5*, which are assumed to generate the most pronounced speract gradients of similar form. This assumption is strictly only valid at the instant of UV exposure, as subsequently the speract gradient dissipates over time with a diffusion constant of $D \approx 240\ \mu m^2 s^{-1}$.

We further sought to understand how the stimulus function, which *S. purpuratus* spermatozoa experience during the accumulation of bound speract throughout their trajectory, influences their motility response. For this purpose, we computed the spatio-temporal dynamics of the speract gradient for *f1, f2, f3, f4* and *f5* fibers (**Figure 4a, 4b** and **S5**) and analyzed the trajectories of spermatozoa swimming in these five distinct speract gradient configurations (**Figure 4c**, **S6a** and **S6c**). Moreover, we computed the stimulus function of individual spermatozoa in response to each of the five speract gradient forms (**Figure 4d**, **S6b, S6d** and **Movie 2**).

From these trajectories, chemotactic behavior was quantified using a novel chemotactic index (CI) (see **Figure 5a)**. This index takes values from -1 (negative chemotaxis) to 1 (positive chemotaxis), being 0 no chemotaxis at all (**Movie 3**). The temporal evolution of the CI, for each of *f1, f2, f3, f4, f5* speract concentration fields, was computed (**Figure 5b)**, and their distributions across time were analyzed by a binomial test (**Figure 5c,** and **Movie S7)**.

The speract field regimes imposed by fibers *f2, f3* and *f5* result in a significant increase of CI, compared to other conditions (*f4*), confirming that the former steeper speract concentration gradients, trigger chemotactic responses on *S. purpuratus* spermatozoa. Again, the lack of chemotactic responses on *S. purpuratus* spermatozoa observed by

Guerrero et al., 2010, was reproduced through stimulation with *f4*, zero Ca^{2+}, or High K^{+} experimental regimes.

The model of chemoreception presented in the previous section (**equations (9)** and **(10)** of **supplementary material**) predicts a scaling rule for chemotactic responses between *S. purpuratus* and *L. pictus* spermatozoa of $SF \sim 3$. Moreover, the derivatives of the UV-irradiation profiles shown in **Figure 2b** indicate that the *f2*, *f3*, and *f5* fibers generate steeper speract gradients than the *f4* fiber.

To reliably determine the direction of the chemoattractant concentration gradient, the signal difference *dc* between two sampled positions *dr* must be greater than the noise (**Figure 1a**). To test the prediction of the chemoreception model, we computed the local relative slope ξ detected by single spermatozoa exposed to a given speract concentration gradient, with $\xi = c^{-1/2} dc/dr$ (**Figure 4d**).

We found that, in agreement with the chemoreception model, the maximum relative slope $\xi_{max} = Max(\xi_1, \xi_2, \xi_3, \ldots, \xi_n)$ required by *S. purpuratus* spermatozoa to perform chemotaxis occurs when exposed to *f2* and *f3* speract gradients, which are up to 2-3 times greater than the one they experience when exposed to the *f4*-generated speract gradient (**Figure 6b**). In addition, *L. pictus* spermatozoa are able to perform chemotaxis when exposed to the *f4* speract gradient, which is 2-3 times smaller than that required by *S. purpuratus* (**Figure 6b**). These findings support the predicted scaling rule for the detection of the speract concentration gradient between *L. pictus* and *S. purpuratus* spermatozoa.

The slope of the speract gradient is the critical determinant for the strength of coupling between the stimulus function and the internal Ca^{2+} oscillator

To test the hypothesis that the slope of the speract gradient regulates the coupling

between the stimulus function and the internal Ca^{2+} oscillator triggered by speract, we made use of a generic model for coupled phase oscillators (Pikovsky et al., 2003). In its simplest form, the model describes two phase oscillators of intrinsic frequencies ω_1 and ω_2 coupled with a strength γ through the antisymmetric function of their phase difference $\phi = \varphi_1 - \varphi_2$. The time evolution of ϕ then follows an Adler equation $d\phi/dt = \Delta\omega - 2\gamma \sin(\phi)$, which is the leading order description for weakly-coupled non-linear oscillators. In the present case, the two coupled oscillators are the internal Ca^{2+} oscillator and the oscillations in the stimulus function induced in spermatozoa swimming across a speract gradient (**Figure 6a**). The former occurs even for immotile cells, for which there are no stimulus oscillations under a spatially uniform speract field (**Figure S7,** and **Movie S8**); while the later exists under two tested negative controls: cells swimming in Low Ca^{2+} and in High K^+ artificial sea water, both of which inhibit Ca^{2+} oscillations (see **Figure 3b, Movie S2** and **S3).**

There are two immediate predictions from the Adler model: first, there is a minimum coupling strength necessary for the two oscillators to synchronize ($\gamma_{min} = \Delta\omega/2$). For weaker coupling (i.e. $\gamma < \gamma_{min}$), the two oscillators run with independent frequencies and, hence, the phase difference increases monotonically with time; second, and within the synchronous region (i.e. $\gamma > \gamma_{min}$), the phase difference between the oscillators is constant and does not take any arbitrary value, but rather follows a simple relation to the coupling strength ($\phi_{sync} = \arcsin(\Delta\omega/2\gamma)$). **Figure 6c** shows the two regions in the parameter space given by $\Delta\omega$ and γ. The boundary between these two regions corresponds to the condition $\gamma = \gamma_{min}$ and it delimits what is known as an Arnold's tongue.

We measured the difference in intrinsic frequency by looking at the instantaneous frequency of the internal Ca^{2+} oscillator just before and after the speract gradient is established. The range of measured $\Delta\omega$ is shown in **Figure 6c** as a band of accessible

conditions in our experiments (mean of $\Delta\omega$, black line; mean ± standard deviation, green dashed lines). If the driving coupling force between the oscillators is the maximum slope of the speract gradient, i.e. $\gamma = \xi_{max}$, we would expect to find a minimum slope ($\overline{\xi^*_{max}}$) below which no synchrony is observed.

This is indeed the case as clearly shown in **Figure 6b**, **6d** and **6e** (magenta line). Moreover, and for cells for which synchronization occurs, the measured phase difference is constrained by the predicted functional form of $\phi_{sync} = \phi_{sync}(\Delta\omega, \gamma)$ as can be verified from the collapsed data shown in **Figure 6d**, and **6e** within the theoretical estimates (see also **Figure S8**).

Altogether, the excellent agreement of this simple model of coupled phase oscillators with our data, points to the slope of the speract gradient as the driving force behind the observed synchronous oscillations and, as a result, for the chemotactic ability of sea urchin spermatozoa.

Discussion

Marine spermatozoa, together with many motile microorganisms, explore their environment via helical swimming paths, whereupon encountering a surface these helices collapse to circular trajectories. The intrinsic periodicity of either swimming behavior commonly results in the periodic sampling of the cell chemical environment with direct implications for their ability to accurately perform chemotaxis.

A strict requirement for sperm chemotaxis is the presence of extracellular Ca^{2+}. For chemotaxis to occur, the timing of the Ca^{2+} transients (i.e. the intracellular Ca^{2+} oscillations) triggered by the chemoattractants must also be kept in phase with the polarity of the chemoattractant concentration field, which in this, and other studies, is referred as the stimulus function (Böhmer et al., 2005; Friedrich and Jülicher, 2008; Guerrero et al., 2010; Kaupp et al., 2008). This requisite coupling ensures that the turning events start at the descending phase of the chemoattractant concentration field; otherwise spermatozoa are driven away by Ca^{2+}-dependent motility adjustments. The periodic sampling of chemoattractants by the sperm flagellum continuously feeds back to the signaling pathway governing the intracellular Ca^{2+} oscillator, hence providing a potential coupling mechanism for sperm chemotaxis. Indirect evidence for the existence of a feedback loop operating between the stimulus function and the Ca^{2+} oscillator triggered by chemoattractants has been found in *L. pictus*, *Arbacia punctulata* and *Ciona intestinalis* species, whose spermatozoa show robust chemotactic responses towards their conspecific chemoattractants (Böhmer et al., 2005; Guerrero et al., 2010; Jikeli et al., 2015; Shiba et al., 2008).

For almost three decades, chemotaxis had not been observed for the widely studied *S. purpuratus* species under diverse experimental conditions, raising doubts about their capabilities to respond to the spatial cues provided by the speract concentration gradients.

To tackle whether *S. purpuratus* spermatozoa are able to derive spatial information from a candidate-chemoattractant concentration gradient, we use a model of chemoreception developed by Berg and Purcell, 1977, which considers the minimal requirements needed for a single searcher (i.e. a sperm cell) to gather sufficient information to determine the orientation of a non-uniform concentration field. By considering the difference between *L. pictus* and *S. purpuratus* spermatozoa in terms of the number of chemoattractant receptors, receptor pocket size, sampling time, swimming velocity, sampling distance, and the local mean and slope of the chemoattractant concentration field, we predicted that *S. purpuratus* should be able to detect the polarity of a speract concentration field. The model predicts that speract gradient necessary to guide *S. purpuratus* spermatozoa would be up to three times steeper than the gradient that drives chemotactic responses on *L. pictus* spermatozoa. We tested this prediction experimentally by exposing *S. purpuratus* spermatozoa to various defined speract concentration gradients. To objectively compare the responses to these gradients we defined a chemotactic index, which incorporates information regarding changes in direction and progressive velocity of the sperm when responding to a chemoattractant gradient (**Figure 5** and **Movie 3**). We show that *S. purpuratus* spermatozoa exhibit chemotactic responses but, as predicted by the chemoreception model, only if the speract concentration gradients are sufficiently steep (i.e. speract gradients that are at least three times steeper than the speract concentration gradient that drives chemotaxis in *L. pictus* spermatozoa). The shallower speract gradients previously tested are therefore unable to generate any chemotactic response in *S. purpuratus* spermatozoa.

To investigate further the molecular mechanism involved in sperm chemotaxis, we measured both the stimulus function and the triggered $[Ca^{2+}]_i$ oscillations for up to one thousand *S. purpuratus* spermatozoa exposed to five distinct speract concentration

gradients. We demonstrate that the slope of the chemoattractant concentration field is a major determinant for sperm chemotaxis in *S. purpuratus* and might be an uncovered feature of sperm chemotaxis in general. A steep slope of the speract gradient entrains the frequencies of the stimulus function and the internal Ca^{2+} oscillator triggered by the periodic sampling of a non-uniform speract concentration field. We assessed the transition boundary of the coupling term (the slope of the speract concentration field) for the two oscillators to synchronize and found it to be very close to the boundary where *S. purpuratus* starts to experience chemotaxis. The agreement of our data with a model of weakly coupled phase oscillators, suggest that the slope of the speract gradient is the driving force behind the observed synchronous oscillations and, as a result, for the chemotactic ability of sea urchin spermatozoa.

One can further hypothesize about the evolutionary origin of the described differences in sensitivity to chemoattractant concentration gradients between *S. purpuratus* and *L. pictus* spermatozoa given the significant dissimilarities between their ecological reproductive niches. The turbulent environment where sea urchin reproduces directly impinges on the dispersion rates of small molecules such as speract, hence, imposing ecological limits that constrain permissive chemoattractant gradient topologies within different hydrodynamic regimes. For instance, the reproduction success of *L. pictus*, *S. purpuratus* and *Abalone* species has been shown to peak at particular hydrodynamic shearing values (Hussain et al., 2017; Mead and Denny, 1995; Riffell and Zimmer, 2007; Zimmer and Riffell, 2011). What are the typical values of the chemoattractant gradients encountered by the different species in their natural habitat? The correct scale to consider when discussing the small-scale distribution of chemicals in the ocean is the Batchelor scale, $l_B = (\eta D^2/\zeta)^{1/4}$, where η is kinematic viscosity, D the molecular diffusivity and ζ is the turbulent dissipation rate (Aref

et al., 2014; Batchelor, 1959). Turbulence stirs dissolved chemicals in the ocean, stretching and folding them into sheets and filaments at spatial dimensions down to the Batchelor scale: below 1_B molecular diffusion dominates and chemical gradients are smoothened out.

S. purpuratus is primarily found in the low intertidal zone. The purple sea urchin lives in an habitat with strong wave action and areas with shaking aerated water. These more energetic zones, including tidal channels and breaking waves, generate relatively high levels of turbulence ($\zeta \sim 10^{-4}$ m^2s^{-3}) which lead to somewhat small values of l_B and, hence, to steep gradients (i.e. l/l_B). *L. pictus*, on the contrary, is mostly found at the edge of or inside kelp beds, well below the low tide mark where the levels of turbulence are much more moderate ($\zeta \sim 10^{-6}$ m^2s^{-3}) (Jiménez, 1997; Thorpe, 2007). This difference in turbulent kinetic energy dissipation rate has a significant effect on the spatial dimensions of chemical gradients for sperm chemotaxis present in a particular habitat. The ratio of l_B for the different habitats scales as $l_{Bpurpuratus}/l_{Bpictus} \sim (\zeta_{pictus}/\zeta_{purpuratus})^{1/4} \sim 3$, which fits considerably well with the relative sensitivity to speract of the two species. Furthermore, we have shown that *S. purpuratus* spermatozoa experience chemotaxis toward steeper speract gradients than those that guide *L. pictus* spermatozoa, which is also compatible with the distinct chemoattractant gradients they might naturally encounter during their voyage searching for the egg.

The chemoattractant concentration gradients generated in the present study were near-instantaneously set up by the photo-release of speract in still water. Further experimental studies are needed to assess the chemotactic ability of sea urchin spermatozoa in more realistic chemoattractant gradients (as those shaped, for instance, by hydrodynamic forces in their natural environment) and to shed light into the mechanisms governing chemotaxis and their ecological implications.

Materials and Methods

Materials

Artificial seawater (ASW), and Low Ca^{2+} ASW were prepared as in (Guerrero et al., 2010), their detailed composition, together with an extended list of other materials is presented in the supplementary materials. Caged speract (CS), was prepared as described previously (Tatsu et al., 2002).

Loading of Ca^{2+}-fluorescent indicator into spermatozoa and microscopy imaging

Undiluted *S. purpuratus* or *L. pictus* were loaded with fluo-4-AM, and their swimming behavior was studied at the water-glass interface on an epifluorescence microscope stage (Eclipse TE-300; Nikon). The cover slips were covered with a poly-HEME to prevent the attachment of the cells to the glass. Images were collected with a Nikon Plan Fluor 40x 1.3 NA oil-immersion objective. Temperature was controlled directly on the imaging chamber at a constant 15 ºC. Stroboscopic fluorescence excitation was provided by a Cyan LED synchronized to the exposure output signal of the iXon camera (2 ms illumination per individual exposure, observation field of 200 x 200 µm), the florescence cube was set up accordingly (see **supplementary material**).

Image processing and quantification of global changes of spermatozoa number and $[Ca^{2+}]_i$

To study the dynamics of overall sperm motility and $[Ca^{2+}]_i$ signals triggered by the distinct speract gradients, we developed an algorithm that provides an efficient approach to automatically detect the head of every spermatozoa in every frame of a given video-microscopy file. A detailed description of the algorithm is provided as supplementary material. Briefly, images are filtered for shot noise, sperm heads are segmented based on global thresholding methods, following by an automatic quantification of head fluorescence and sperm trajectories. Up to 267 videos of *S. purpuratus* spermatozoa, each containing

tens of swimming cells, exposed to five distinct speract concentration gradients, were automatically analyzed.

Computing the dynamics of speract concentration gradients

The dynamics of the chemoattractant gradient was computed using Green's function of the diffusion equation:

$$c(r,t) = \frac{C_0}{\sqrt{2\pi\sigma}} e^{-r^2/2\sigma^2} + C_b \quad (3)$$

This equation for the concentration tells us that the profile has a Gaussian form. The width of the Gaussian is $\sigma = \sqrt{4D(t+t_0)}$, and hence it increases as the square root of time. C_b is the basal concentration of the chemoattractant, D is the molecular diffusivity.

The speract concentration gradients were generated via the photolysis of 10 nM caged speract (CS) with a 200 ms UV pulse delivered through each of four different optical fibers with internal diameters of 200 µm, 600 µm, 2 mm and 4 mm (at two different positions). Light intensity was normalized dividing each point by the sum of all points of light intensity for each fiber and multiplying it by the fiber potency (measured at the back focal plane of the objective) in miliwatts (mW) (**Table S2**). Each spatial distribution of instantaneously-generated speract concentration gradient was computed by fitting their corresponding normalized spatial distribution of UV light (Residual standard error: 2.738 x 10^{-5} on 97 degrees of freedom), considering an uncaging efficiency of 5%, as reported (Tatsu et al., 2002).

The diffusion coefficient of a molecule is related to its size by the Stokes-Einstein equation: $D = \frac{kT}{6\pi\eta R_h}$, where k is Boltzmann's constant, T is the temperature, η is the viscosity of the solvent, and R_h is the hydrodynamic radius (Lakowicz, 2006). The hydrodynamic radius R_h of speract was calculated by modeling the molecules in terms of

equivalent hydrodynamic spheres. $R_h = \left(\frac{3M\bar{v}}{4\pi}\right)^{1/3}$, where M is the molecular weight, and $\bar{v}$ is the specific gravity (Lakowicz, 2006). The volume of an equivalent spherical particle is $V_e = 4/3\,\pi R_h^3$. These equations show that the radius and diffusion coefficient are weakly dependent on the molecular weight.

The diffusion coefficient of speract has not been measured experimentally, nonetheless it can be estimated following equations **6** and **7 (supplementary material)**. The diffusion coefficient of a similar chemoattractant molecule, resact (with fourteen amino acids), has been reported, D_{resact} = 239 ± 7 μm^2 s^{-1} (Kashikar et al., 2012). If we consider that speract is a decapeptide, the 1.4 fold difference in molecular weight between speract and resact would imply a $(1.4)^{1/3}$ fold difference in their diffusion coefficients, which is close to the experimental error reported (Kashikar et al., 2012). For the sake of simplicity, the spatio-temporal dynamics of the distinct instantaneously generated speract gradients was modeled considering a speract diffusion coefficient of $D_{speract}$ = 240 μm^2 s^{-1}.

The hydrodynamic radius of speract (R_h = 8.8 Å) was computed with $D_{speract}$ = 240 μm^2 s^{-1}, k = 1.38 x 10^{-23} J K^{-1}, T = 288.15 K and η = 0.001 N s /m^2.

Computing $[Ca^{2+}]_i$ dynamics and the stimulus function of single spermatozoa

Spermatozoa were tracked semi-automatically by following the head centroid with the MtrackJ plugin (Meijering et al., 2012) of ImageJ 1.49u. Single cell $[Ca^{2+}]_i$ signals were computed from the mean value of a 5 x 5 pixel region, centered at each sperm head along the time. The head position of each spermatozoa was used to compute the local concentration of speract at $r(x, y)$ over each frame. The stimulus function of single spermatozoa $s = c(r, t)$ was computed by solving equation (**3**), considering both their swimming trajectories, and the spatio-temporal evolution of a given speract concentration

gradient. The profiles of UV light were used to compute the initial conditions at $c(r, t_o)$.

The phase- and temporal-shifts between time derivative of the stimulus function ds/dt and the internal Ca^{2+} oscillator triggered by speract, were computed from their normalized cross-correlation function.

Programs were written in R statistical software.

Chemotactic index

Each sperm trajectory was smoothened using a moving average filter, with a window of 60 frames (two seconds approximately) (**Figure 5a and Movie 3**). A linear model was then fitted to the smoothed trajectory, the corresponding line was forced to go through the mean point of the smoothed trajectory (orange point in **Figure 5a and Movie 3**). The θ angle between red and black vectors was calculated in each frame from the second 4.5 to 10.

The chemotactic index was defined based on the progressive displacement of the sperm trajectory as $CI = \frac{|u|cos\theta - |v|cos\varphi}{|u|+|v|}$, being ϕ and θ the angles between gray and magenta, and red and black vectors, respectively; and |*v*| and |u| the magnitude of the sperm progressive velocity before and after speract uncaging, respectively (**Figure 5a and Movie 3**). The CI considers the sperm displacement before speract uncaging (i.e. unstimulated drift movement at 0-3 seconds), and then subtracts it from the speract induced effect (at 3-10 seconds). The CI takes values from -1 (negative chemotaxis) to 1 (positive chemotaxis), being 0 no chemotaxis at all.

Statistical analyses

The normality of the *CI* distributions, each obtained from *f1* to *f5* speract gradient stimuli, was first assessed using the Shapiro-Wilk test; none of them were normal (Gaussian), so each *CI* distribution was analyzed using non-parametric statistics **(Movie S7)**. The curves

obtained from medians of each *CI* distribution were smoothed using a moving average filter, with a window of 20 frames (0.6 seconds).

Data are presented for individual spermatozoa (n) collected from up to three sea urchins. All statistical tests were performed using R software (R Development Core Team, 2016). The significance level was set at 95%.

Acknowledgements

The authors thank Dr. Tatsu Yoshiro for providing the caged speract, and Drs. Hermes Gadêlha, David Smith and Nina Pastor for stimulating discussions and a critical reading of the manuscript. AG thanks Dr. Manabu Yoshida and Dr. Kaoru Yoshida for feedback regarding sperm chemotaxis in marine invertebrates, and to the Japan Society for the Promotion of Science (JSPS invitation fellowship for research in Japan to A.G., short term JSPS/236, ID no. S16172).

Author contributions

A.G., A.D. and I.T. conceived the project; A.G. and V.J.S. performed the experiments; H.R., A.G., I.T., V.J.S. and M.V. analyzed the data; A.G., I.T. and H.R. performed the mathematical model calculations and wrote the corresponding section; H.R. and I.T. developed the chemotactic index; A.D., A.G., H.R. and I.T. participated in the design and drafting of the manuscript; J.C., C.D.W. and C.B. provide feedback for conceptualization and drafting of the manuscript. All authors approved the final version of the article.

Competing interests

The authors declared that no competing interests exist.

Funding

A.D. and A.G. acknowledge grants from the Consejo Nacional de Ciencia y Tecnología (CONACyT Fronteras 71, CONACyT Ciencia Básica 252213 and CONACyT 255914), A.G., A.D. and C.B to Programa de Apoyo a Proyectos de Investigación e Innovación Tecnológica UNAM (PAPIIT/DGAPA) (IA202417, IN205516, IN206016 and IN112514). We acknowledge CONACYT and PAPIIT for fellowships to M.V.P. and H.R.; the Spanish Ministry of Economy and Competitiveness Grants No. FIS2013-48444-C2-1-P, FIS2016-77692-C2-1- P, the Subprogram Ramón-y-Cajal and the Ibero-America Program-Santander Universities 2015 (I.T.).

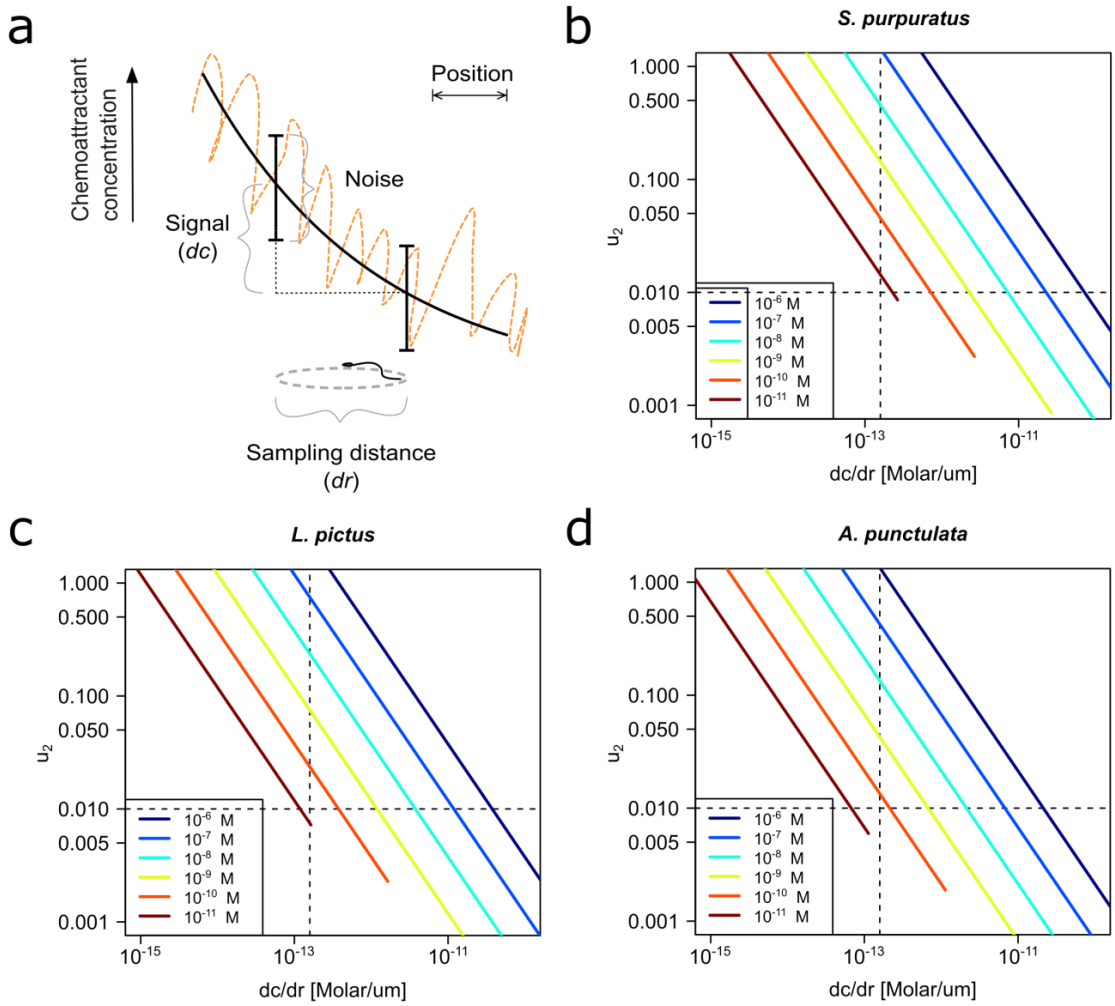

Figure 1. Physics of chemoreception. a. Determining the direction of the chemoattractant gradient requires that the signal difference *dc* between two sampled positions *dr* must be greater than the noise. **b-d.** The uncertainty in the determination of the chemoattractant gradient direction, u_2, plotted against the slope of the gradient, *dc/dr*, in log-log scale, for different chemoattractant concentrations: **(b)** *S. purpuratus*, **(c)** *L. pictus*, and **(d)** *A. punctulata* spermatozoa (See **Table S1** for the list of parameter values taken in consideration for panels **b-d**). Note that functions in panels **b-d** are truncated, because a locality requirement, given by $t_{int}\frac{d\log c}{dr} \ll 1$, must be met (see **Theory 2.4. Uncertainty in the detection of a chemoattractant concentration fields**, in **supplementary material**).

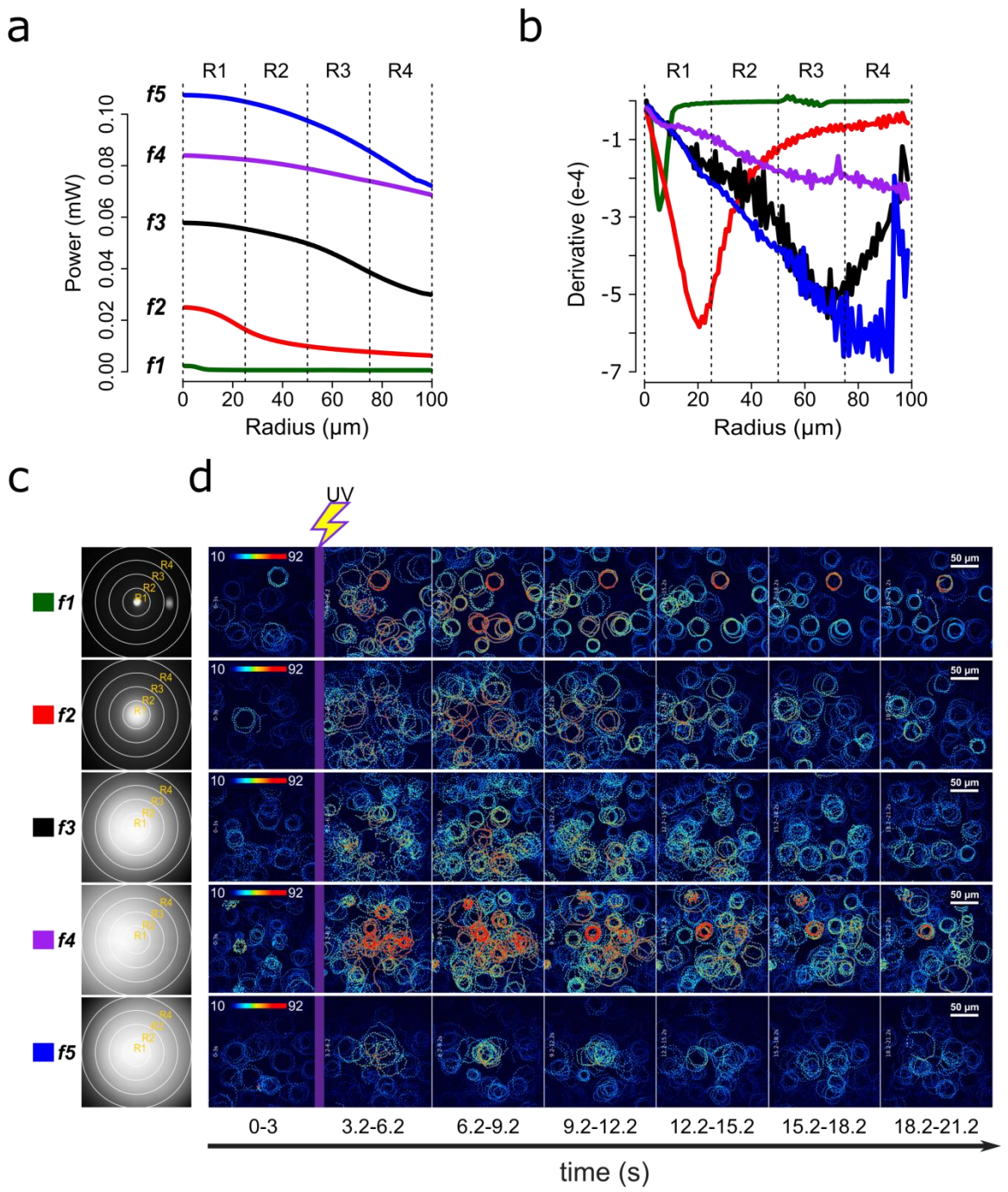

Figure 2. Screening of speract concentration gradients. a. Radial profile of the UV light scattered at the glass-liquid interface for each optical fiber (*f1-f5*). **b**. Derivatives of radial distribution for each optical fiber. **c**. Spatial distribution of the UV flash energy for each fiber. **d.** Representative motility and $[Ca^{2+}]_i$ responses of spermatozoa exposed to different

concentration gradients of speract. $F-F_0$ time projections, showing spermatozoa head fluorescence at 3 s intervals before and after photoactivation of 10 nM caged speract in artificial seawater with 200 ms UV. The pseudo-color scale represents the relative fluorescence of fluo-4, an $[Ca^{2+}]_i$ indicator, showing maximum (red) and minimum (blue) relative $[Ca^{2+}]_i$. Scale bars of 50 µm.

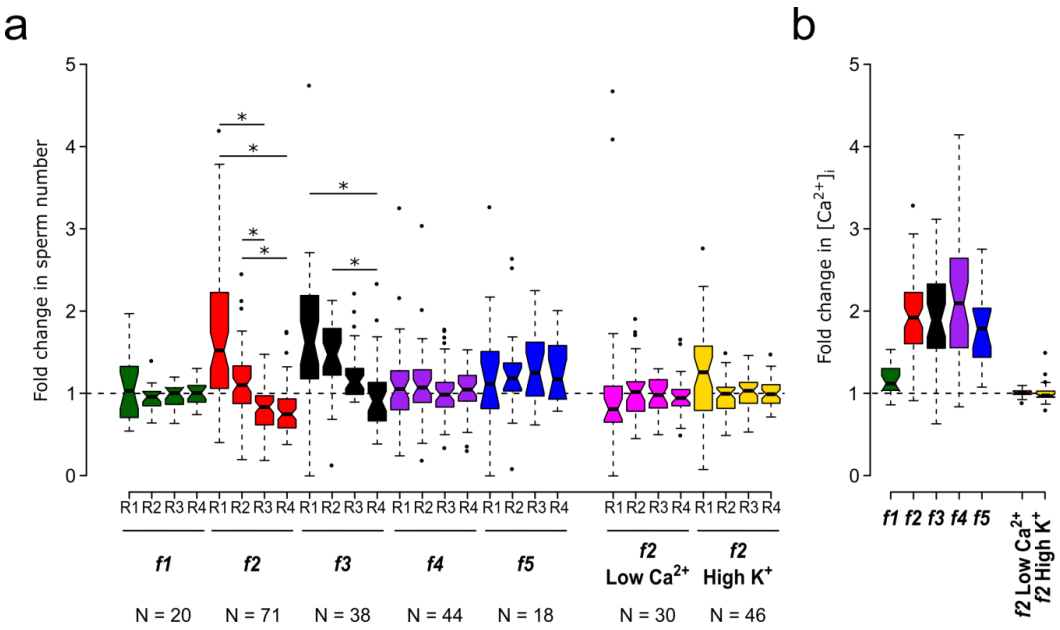

Figure 3. Motility and $[Ca^{2+}]_i$ responses of *S. purpuratus* spermatozoa exposed to specific concentration gradients of speract. a. Fold change in sperm number, defined as the number of spermatozoa at the peak of the response (6 s) relative to the mean number before speract stimulation (0-3 s) (see **Figure S4**). **b**. Relative changes in $[Ca^{2+}]_i$ experienced by spermatozoa at the peak response (6 s) after speract stimulation. Negative controls for spermatozoa chemotaxis are artificial seawater with nominal Ca^{2+} (Low Ca^{2+}); and artificial seawater with 40 mM of K^+ (High K^+). Both experimental conditions prevent chemotactic responses by inhibiting the Ca^{2+} membrane permeability alterations triggered by speract; the former disrupts the Ca^{2+} electrochemical gradient, and the later disrupt the K^+ electrochemical gradient required as electromotive force needed for the opening of Ca^{2+} channels. The central line represents the median value, the box denotes the data spread from 25 and 75%, and the whiskers reflect 10–90%. Number of experiments (N) is indicated on the bottom of each experimental condition. We used the same N for the relative change in $[Ca^{2+}]_i$ (right panel). *Statistical significance, $p < 0.05$; multiple comparison test after Kruskal-Wallis.

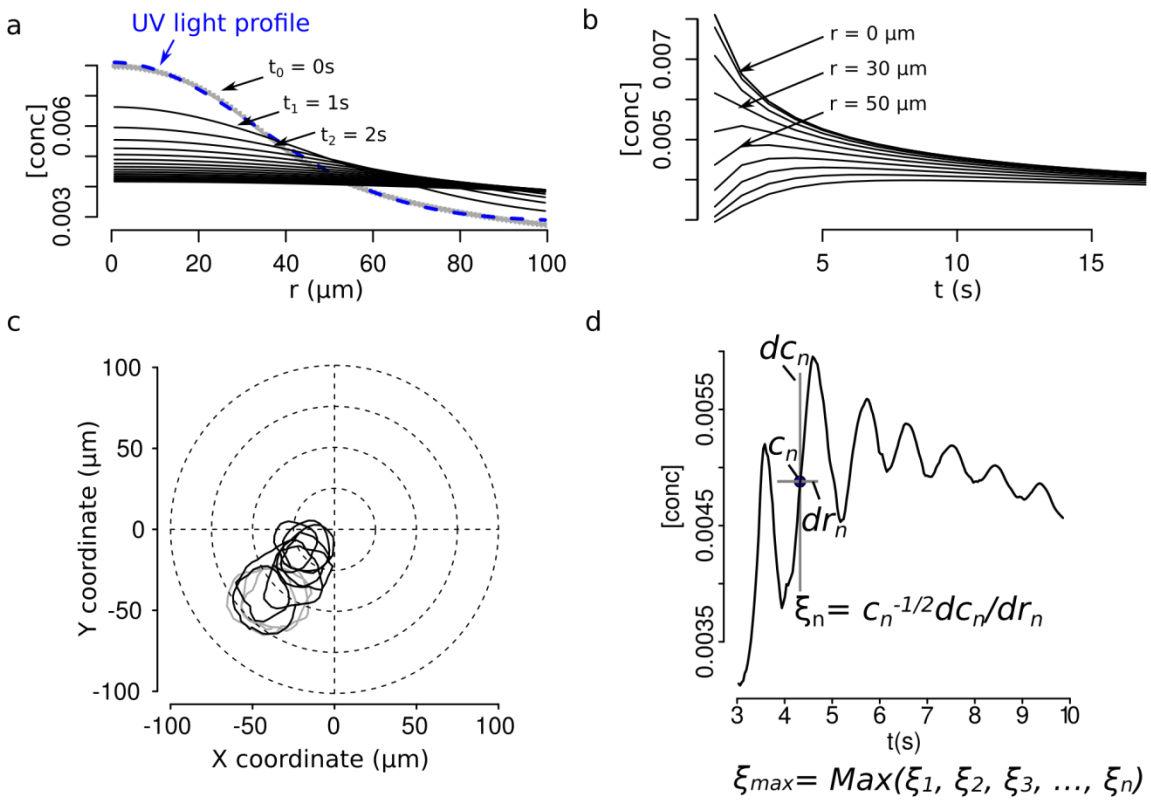

Figure 4. Steep speract gradients attract *S. purpuratus* spermatozoa. a. Dynamics of the *f2* speract gradient. The blue dashed line (t_0 = 0 s) corresponds to a Gaussian distribution fitted to the UV light profile and illustrates the putative shape of the instantaneously-generated speract concentration gradient. Solid black lines illustrate the temporal evolution of the speract concentration field after t = 1, 2, 3, …, 20 seconds. **b.** Temporal changes in the *f2* speract field computed radially (each 10 μm) from the center of the gradient. **c.** Characteristic motility changes of a *S. purpuratus* spermatozoon exposed to the *f2* speract gradient. Solid lines illustrate its swimming trajectory 3 s before (gray) and 6 s after (black) speract exposure. **d**. Stimulus function computed from the swimming behavior of the spermatozoon in **c**, considering the dynamics of **a**.

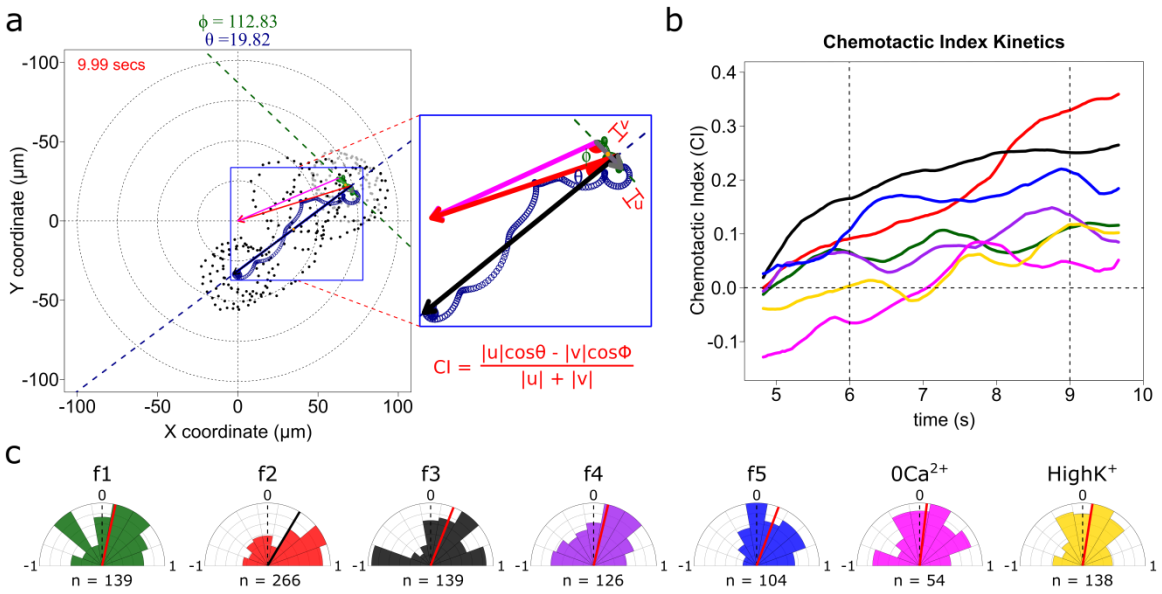

Figure 5. *S. purpuratus* spermatozoa selectively experience chemotaxis towards specific speract gradients. a. Definition of a chemotactic index to score chemotactic responses. Dots represent sperm trajectory before (gray) and after (black) UV irradiation. Green and blue empty circles indicated the smoothed trajectory before and after UV irradiation. Grey and black vectors are the progressive sperm displacement before and after stimulation, respectively; and **v** and **u** vectors are the linear/progressive velocity before and after stimulation; and ϕ and θ are the angles to their corresponding reference vectors to the center of the imaging field – the highest UV irradiated area, (magenta and red, respectively). Chemotactic index (CI) is defined as in the inset, where **v** and **u** are the speeds obtained for the trajectories before and after UV flash, respectively (**Movie 3**). **b.** Temporal evolution of the chemotactic index. Functions were calculated from the median obtained from more than 50 sperm trajectories of each of *f1, f2, f3, f4, f5, f2-ZeroCa*$^{2+}$, and *f2-HighK*$^{+}$ experimental conditions (**Movie S7**). **c.** Radial histograms at second 9 (vertical dotted line at panel **b**). Significant differences (*Binomial test, p-value* < *0.05*) were observed only for *f2*, *f3* and *f5* fibers, compared to controls.

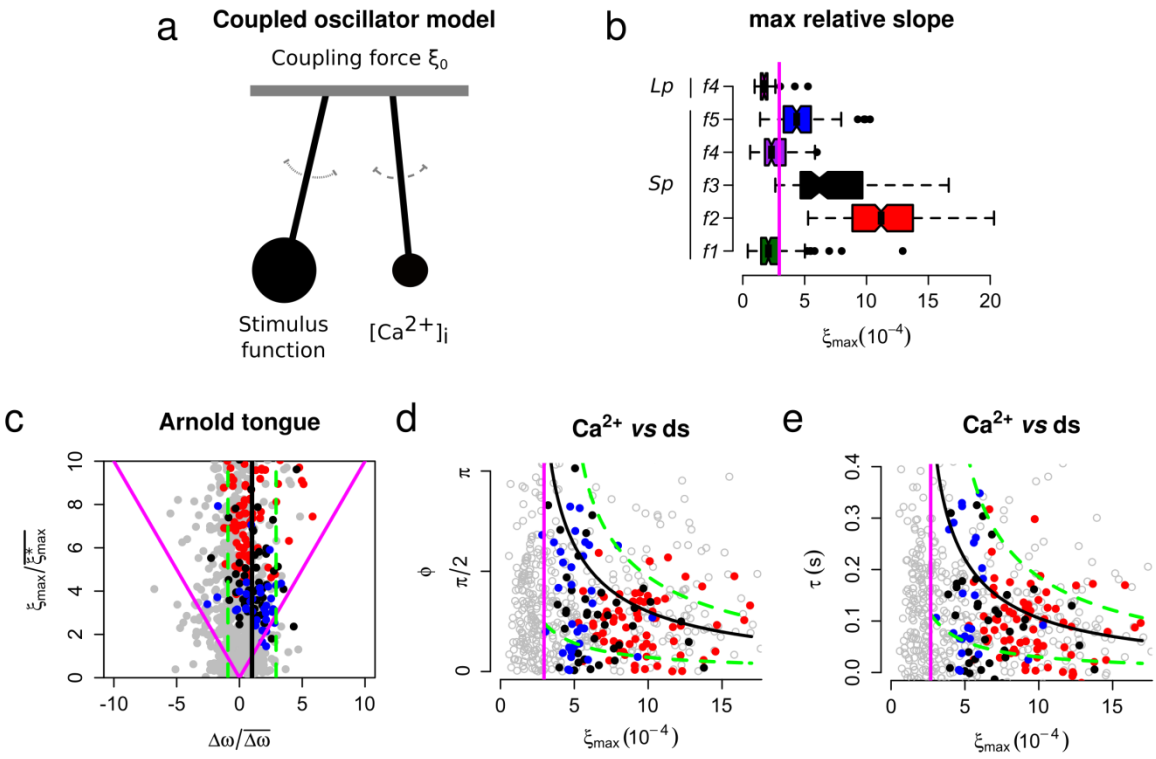

Figure 6. The slope of the speract gradient generates a frequency-locking phenomenon between the stimulus function and the internal Ca^{2+} oscillator triggered by speract. a. Coupled oscillator model. Each sperm has two independent oscillators: i) Stimulus function and ii) $[Ca^{2+}]_i$, which can be coupled through a forcing term which connects them, in our case the slope of the chemoattractant gradient (ξ_0). **b.** Maximum relative slopes (ξ_{max}) experienced by *S. purpuratus* (*Sp*) spermatozoa when exposed to *f1, f2, f3, f4, f5* speract gradients. The maximum relative slopes experienced by *L. pictus* spermatozoa (*Lp*) towards *f4* experimental regime are also shown. Note that ξ_{max} for *f2, f3,* and *f5*, are up to 2-3 times greater than in *f4*, regardless of the species. **c.** Arnold's tongue indicating the difference in intrinsic frequency of the internal Ca^{2+} oscillator of *S. purpuratus* spermatozoa, just before and after the speract gradient exposure. **d**. Phase difference between the time derivative of the stimulus function and the internal Ca^{2+} oscillator of *S. purpuratus* spermatozoa, obtained by computing the cross-correlation

function between both time series (**Figure S8**). **e**. Phase difference between the time derivative of the stimulus function and the internal Ca^{2+} oscillator of *S. purpuratus* spermatozoa expressed in temporal delays. **c-e**. Gray points represent the collapsed data of all *f1, f2, f3, f4, f5* experimental regimes. Red, black and blue points indicate chemotactic spermatozoa (CI > 0 at -second 3 after UV flash), located in R3, and R4 regions just before the speract gradient is established under *f2*, *f3* and *f5* experimental regimes, respectively. Magenta lines represent the transition boundary ($\gamma_{min} = \overline{\xi^*_{max}} \sim 2.7 \times 10^{-4}$) below which no synchrony is observed, obtained from the theoretical estimates (black curves, mean of $\Delta\omega$) of panels **d** and **e**. Green dashed lines indicate confidence intervals (mean ± standard deviation).

https://www.dropbox.com/s/oe0mnc8j5r65l8s/Movie%201.avi?dl=0

Movie 1. Typical motility and Ca^{2+} responses of *S. purpuratus* spermatozoa towards an *f2*-generated speract concentration gradient. Spermatozoa swimming in artificial sea water containing 10 nM caged speract, 3 s before and 5 s after 200 ms UV irradiation. An optical fiber of 0.6 mm internal diameter was used for the UV light path to generate the speract concentration gradient. Real time: 31 frames s^{-1}, 40x /1.3NA oil-immersion objective. Note that spermatozoa located at R2, R3 and R4 regions prior to speract exposure swim up the speract concentration gradient, towards the center of the imaging field (R1). The pseudo-color scale represents the relative fluorescence of fluo-4, a Ca^{2+} indicator, showing maximum (red) and minimum (blue) relative $[Ca^{2+}]_i$. Six *S. purpuratus* spermatozoa were manually tracked for visualization purposes. Scale bar = 50 µm.

https://www.dropbox.com/s/gtvau67qlaoriwj/Movie%202.1.avi?dl=0

Movie 2. Sperm trajectory analysis and stimulus function. Single-cell analysis was performed for approximately 1000 sperm trajectories for the different speract gradients (*f1-f5* and negative controls). The sperm trajectory shown here represents a chemotactic sperm. This analysis was implemented after the speract uncaging (from 3.2-10 seconds), speract uncaging was induced at second 3. Trajectory before, after and during the 200 ms UV flash is shown in gray, black and purple, respectively.

https://www.dropbox.com/s/tbqsyjjnq7ilbwm/Movie%203.1.avi?dl=0

Movie 3. Sperm trajectory analysis and chemotactic index. Single-cell analysis was performed for approximately 1000 sperm trajectories from the different speract gradients (*f1-f5* and controls). Angle ϕ is calculated just once and is always the same for each sperm trajectory. Angle θ is calculated per frame of the video for each sperm trajectory, resulting in the chemotactic index kinetics for each sperm trajectory (right panel). The sperm trajectory shown here represents a chemotactic sperm. This analysis was implemented from 4.5 seconds to 10 seconds. Speract uncaging was induced at 3 seconds. Trajectory before and after speract release is shown in gray and black dots, respectively.

References

Aguilera LU, Galindo BE, Sánchez D, Santillán M. 2012. What is the core oscillator in the speract-activated pathway of the Strongylocentrotus purpuratus sperm flagellum? *Biophys J* **102**:2481–2488. doi:10.1016/j.bpj.2012.03.075

Alvarez L, Dai L, Friedrich BM, Kashikar ND, Gregor I, Pascal R, Kaupp UB. 2012. The rate of change in Ca(2+) concentration controls sperm chemotaxis. *J Cell Biol* **196**:653–63. doi:10.1083/jcb.201106096

Aref H, Blake JR, Budišić M, Cardoso SSS, Cartwright JHE, Clercx HJH, Omari K El, Feudel U, Golestanian R, Gouillart E, van Heijst GF, Krasnopolskaya TS, Guer Y Le, MacKay RS, Meleshko V V., Metcalfe G, Mezić I, de Moura APS, Piro O, Speetjens MFM, Sturman R, Thiffeault J-L, Tuval I. 2014. Frontiers of chaotic advection. *Rev Mod Phys* **89**:025007. doi:10.1103/RevModPhys.89.025007

Batchelor GK. 1959. Small-scale variation of convected quantities like temperature in turbulent fluid Part 1. General discussion and the case of small conductivity. *J Fluid Mech* **5**:134. doi:10.1017/S0022112059000106

Berg HC, Purcell EM. 1977. Physics of chemoreception. *Biophys J* **20**:193–219. doi:10.1016/S0006-3495(77)85544-6

Böhmer M, Van Q, Weyand I, Hagen V, Beyermann M, Matsumoto M, Hoshi M, Hildebrand E, Kaupp UB, Bohmer M, Van Q, Weyand I, Hagen V, Beyermann M, Matsumoto M, Hoshi M, Hildebrand E, Kaupp UB. 2005. Ca2+ spikes in the flagellum control chemotactic behavior of sperm. *EMBO J* **24**:2741–52. doi:10.1038/sj.emboj.7600744

Brokaw CJ. 1979. Calcium-induced asymmetrical beating of triton-demembranated sea urchin sperm flagella. *J Cell Biol* **82**:401–411. doi:10.1083/jcb.82.2.401

Cook SP, Brokaw CJ, Muller CH, Babcock DF. 1994. 1994 Dev Biol, Cook - Sperm chemotaxis, Egg peptides control cytosolic calcium to regulate flagellar responses.pdf. *Dev Biol* **165**:10–19. doi:10.1006/dbio.1994.1229

Darszon A, Guerrero A, Galindo BE, Nishigaki T, Wood CD. 2008. Sperm-activating peptides in the regulation of ion fluxes, signal transduction and motility. *Int J Dev Biol* **52**:595–606. doi:10.1387/ijdb.072550ad

Dusenbery DB. 2011. Living at micro scale, First. ed. Harvard University Press.

Espinal J, Aldana M, Guerrero A, Wood C, Darszon A, Martínez-Mekler G, Martinez-Mekler G, Martínez-Mekler G. 2011. Discrete dynamics model for the speract-activated Ca2+ signaling network relevant to sperm motility. *PLoS One* **6**:e22619. doi:10.1371/journal.pone.0022619

Friedrich BM, Jülicher F. 2009. Steering chiral swimmers along noisy helical paths. *Phys Rev Lett* **103**:1–4. doi:10.1103/PhysRevLett.103.068102

Friedrich BM, Jülicher F. 2008. The stochastic dance of circling sperm cells: sperm chemotaxis in the plane. *New J Phys* **10**:123025. doi:10.1088/1367-2630/10/12/123025

Friedrich BM, Jülicher F. 2007. Chemotaxis of sperm cells. *Proc Natl Acad Sci U S A* **104**:13256–13261. doi:10.1073/pnas.0703530104

Guerrero A, Nishigaki T, Carneiro J, Yoshiro Tatsu, Wood CD, Darszon A. 2010. Tuning sperm chemotaxis by calcium burst timing. *Dev Biol* **344**:52–65. doi:10.1016/j.ydbio.2010.04.013

Guerrero A, Wood CD, Nishigaki T, Carneiro J, Darszon A. 2010. Tuning sperm

chemotaxis. *Biochem Soc Trans* **38**:1270–4. doi:10.1042/BST0381270
Hansbrough JR, Garbers DL. 1981. Speract. Purification and characterization of a peptide associated with eggs that activates spermatozoa. *J Biol Chem* **256**:1447–1452.
Hussain YH, Sadilek M, Salad S, Zimmer RK, Riffell JA. 2017. Individual female differences in chemoattractant production change the scale of sea urchin gamete interactions. *Dev Biol* **422**:186–197. doi:10.1016/j.ydbio.2017.01.006
Jikeli JF, Alvarez L, Friedrich BM, Wilson LG, Pascal R, Colin R, Pichlo M, Rennhack A, Brenker C, Kaupp UB. 2015. Sperm navigation along helical paths in 3D chemoattractant landscapes. *Nat Commun* **6**:7985. doi:10.1038/ncomms8985
Jiménez J. 1997. Oceanic turbulence at millimeter scales. *Sci Mar* **61**:47–56.
Kashikar ND, Alvarez L, Seifert R, Gregor I, Jäckle O, Beyermann M, Krause E, Kaupp UB, Benjamin Kaupp U, Kaupp UB, Benjamin Kaupp U. 2012. Temporal sampling, resetting, and adaptation orchestrate gradient sensing in sperm. *J Cell Biol* **198**:1075–91. doi:10.1083/jcb.201204024
Kaupp UB. 2012. 100 Years of Sperm Chemotaxis. *J Gen Physiol* **140**:583–586. doi:10.1085/jgp.201210902
Kaupp UB, Kashikar ND, Weyand I. 2008. Mechanisms of sperm chemotaxis. *Annu Rev Physiol* **70**:93–117. doi:10.1146/annurev.physiol.70.113006.100654
Kaupp UB, Solzin J, Hildebrand E, Brown JE, Helbig A, Hagen V, Beyermann M, Pampaloni F, Weyand I. 2003. The signal flow and motor response controling chemotaxis of sea urchin sperm. *Nat Cell Biol* **5**:109–117. doi:10.1038/915
Lakowicz JR. 2006. Principles of Fluorescence Spectroscopy Principles of Fluorescence Spectroscopy, Principles of fluorescence spectroscopy, Springer, New York, USA, 3rd edn, 2006. doi:10.1007/978-0-387-46312-4
Lillie FR. 1913. The mechanism of fertilization **38**:524–528.
Lotterhos K, Levitan D, Traits G. 2010. Gamete release and spawning behavior in broadcast spawning marine invertebrates. *Evol Prim Sex Characters Anim* 99–120.
Mead KS, Denny MW. 1995. The effects of hydrodynamic shear stress on fertilization and early development of the purple sea urchin Strongylocentrotus purpuratus. *Biol Bull* **188**:46–56. doi:10.2307/1542066
Meijering E, Dzyubachyk O, Smal I. 2012. Methods for cell and particle tracking. *Methods Enzym* **504**:183–200. doi:10.1016/B978-0-12-391857-4.00009-4
Miller RL. 1985. Sperm Chemo-Orientation in the Metazoa In: Metz CB, Monroy A, editors. Biology of Fertilization. New York: Academic Press. pp. 275–337.
Nishigaki T, Darszon a. 2000. Real-time measurements of the interactions between fluorescent speract and its sperm receptor. *Dev Biol* **223**:17–26. doi:10.1006/dbio.2000.9734
Nishigaki T, Zamudio FZ, Possani LD, Darszon A. 2001. Time-Resolved Sperm Responses to an Egg Peptide Measured by Stopped-Flow Fluorometry. *Biochem Biophys Res Commun* **284**:531–535. doi:10.1006/bbrc.2001.5000
Pfeffer W. 1884. Locomotorische Richtungsbewegungen durch chemische Reize. *Untersuchungen aus dem Bot Inst zu Tübingen*.
Pichlo M, Bungert-Plümke S, Weyand I, Seifert R, Bönigk W, Strünker T, Kashikar ND, Goodwin N, Müller A, Pelzer P, Van Q, Enderlein J, Klemm C, Krause E, Trötschel C, Poetsch A, Kremmer E, Kaupp UB. 2014. High density and ligand affinity confer ultrasensitive signal detection by a guanylyl cyclase chemoreceptor. *J Cell Biol* **206**:541–57. doi:10.1083/jcb.201402027

Pikovsky A, Rosenblum M, Kurths J. 2003. Synchronization: A Universal Concept in Nonlinear Sciences. *Cambridge Nonlinear Sci Ser 12* 432. doi:10.1063/1.1554136

R Development Core Team. 2016. R Development Core Team.

Riffell J a, Zimmer RK. 2007. Sex and flow: the consequences of fluid shear for sperm-egg interactions. *J Exp Biol* **210**:3644–3660. doi:10.1242/jeb.008516

Shiba K, Baba S a, Inoue T, Yoshida M. 2008. Ca2+ bursts occur around a local minimal concentration of attractant and trigger sperm chemotactic response. *Proc Natl Acad Sci U S A* **105**:19312–7. doi:10.1073/pnas.0808580105

Strünker T, Alvarez L, Kaupp UB. 2015. At the physical limit - chemosensation in sperm. *Curr Opin Neurobiol* **34**:110–116. doi:10.1016/j.conb.2015.02.007

Suzuki N. 1995. Structure, function and biosynthesis of sperm-activating peptides and fucose sulfate glycoconjugate in the extracellular coat of sea urchin eggs. *ZoologSci* **12**:13–27.

Tatsu Y, Nishigaki T, Darszon A, Yumoto N. 2002. A caged sperm-activating peptide that has a photocleavable protecting group on the backbone amide. *FEBS Lett* **525**:20–24.

Thorpe S. 2007. An introduction to ocean turbulence. Cambridge University Press.

Wood C, Guerrero A, Priego-espinosa DA, Martĭnez-mekler G, Carneiro J, Darszon A. 2015. CHAPTER 2 Sea Urchin Sperm Chemotaxis 135–182.

Wood CD, Darszon A, Whitaker M. 2003. Speract induces calcium oscillations in the sperm tail. *J Cell Biol* **161**:89–101. doi:10.1083/jcb.200212053

Wood CD, Nishigaki T, Furuta T, Baba S a, Darszon A. 2005. Real-time analysis of the role of Ca(2+) in flagellar movement and motility in single sea urchin sperm. *J Cell Biol* **169**:725–31. doi:10.1083/jcb.200411001

Wood CD, Nishigaki T, Tatsu Y, Yumoto N, Baba SA, Whitaker M, Darszon A. 2007. Altering the speract-induced ion permeability changes that generate flagellar Ca2+ spikes regulates their kinetics and sea urchin sperm motility. *Dev Biol* **306**:525–537. doi:10.1016/j.ydbio.2007.03.036

Zimmer RK, Riffell JA. 2011. Sperm chemotaxis, fluid shear, and the evolution of sexual reproduction. *Proc Natl Acad Sci* **108**:13200–13205. doi:10.1073/pnas.1018666108